Study of Flow Induced by Nonuniform Lateral Injection

M.-K. Tsai* and T.-M. Liou†
National Tsing Hua University, Hsin-Chu, Taiwan 30043, Republic of China

The cold flowfield in a closed-end 90 m-porosity porous-walled two-dimensional duct at nonuniform lateral injection condition (approximately exponential distribution) has been investigated, using both laser-Doppler velocimetry measurements and theoretical analysis. The measured and predicted similar velocity profiles are in reasonable agreement, and the conditions for the existence of similarity are identified. A comparison with the previous case of uniform wall injection has also been made. The comparison includes the transition process of the mean-velocity profile, the shift of peak turbulence intensity, the evolution of relative turbulence intensity with axial distance, and the sensitivity of the local heat transfer or erosive burning rate to the relative injection ratio.

Nomenclature

C_p = pressure-loss coefficient
f = the $f(y)$ function in $\Psi(x, y)$
g = the $g(x)$ function in $\Psi(x, y)$
h = channel half-height
$\hbar$ = convective heat transfer coefficient
I = turbulence intensity, $= (u^2 + v^2)^{1/2}$
L = channel length
M = Mach number
P = local static pressure
$\mathcal{P}$ = pressure drop from head end, i.e., $(P_o - P)$
R_a = gas constant of air
R_c = centerline axial Reynolds number, $= U_c h/\nu$
R_w = wall suction/injection Reynolds number, $= V_w h/\nu$ (positive for suction, negative for injection)
R_{wi} = injection Reynolds number, $= -V_w h/\nu$
U = axial mean velocity
u = axial turbulence intensity
V = transverse mean velocity
V_w = wall suction/injection velocity (positive for suction, negative for injection)
V_{wi} = wall injection velocity, i.e., $-V_w$
v = transverse turbulence intensity
W = channel half-width
X = X-coordinate
x = dimensionless X-coordinate, $= X/h$
x_1 = location where velocity similarity begins
Y = Y-coordinate
Y' = distance from wall, $= (h - Y)$
y = dimensionless Y-coordinate, $= Y/h$
y' = dimensionless Y'-coordinate, $= Y'/h$
β = momentum flux factor, $= 1/U_b^2 \int_0^1 U^2 dy$
β_e = constant in Eq. (4)
ν = air dynamic viscosity
ρ = air density
σ_v = surface generated pseudoturbulence, $= (\overline{v^2}/V^2)_w^{1/2}$
Ψ = stream function

Superscripts
$'$ = differentiation
$-$ = average value

Subscripts
o = head-end, i.e., location $x = 0$
1 = location x_1
b = bulk mean value (cross-sectionally)
c = centerline, i.e., X-axis
i = injection
p = location of peak turbulence intensity
w = wall

Introduction

THE flowfield in a duct with fluid injected or sucked-through porous walls are often encountered in practical applications. Examples are transpiration cooling, flow filtration, boundary-layer control, and the combustion-induced flowfield in solid-rocket motors (SRM).[1-7] In order to understand the relevant processes involved in these applications, it is first necessary to understand the detailed fluid flow characteristics. This paper is concerned with the SRM internal flowfield.

In the internal flowfield of an SRM, early attempts were mainly concerned with the distribution of mean velocities. Based on inviscid Euler equation and potential flow theory, Culick[1] derived the velocity profiles for flows in a closed head-end cylinder subjected to the boundary condition of uniform injection normal to the cylindrical surface. Subsequently, Dunlap et al.[2] verified Culick's solution by hot-wire measurements, and showed that injection-induced flow, especially at high R_{wi}, was turbulent, yet, the mean-velocity profile maintained its laminar form. They further concluded that the contribution of Reynolds stress to the mean axial momentum equation was negligible for this type of flow. The resulting momentum balance was predominantly inviscid (i.e., Euler equations are valid). Thus, maintaining the laminar velocity profile and verifying the applicability of the inviscid fluid solution to the real flow resulted. For the tube with a closed end and uniform wall injection, the induced turbulent flow had the feature of maintaining the mean-velocity profiles in the laminar form. The transition of this type flows from laminar similar to the real turbulent form, therefore becoming interesting. The transition especially was found to occur prior to the onset of erosive burning in the SRM grain port.[5] Varapaev and Yagodkin[8] performed a linear viscous stability analysis on uniform injection-induced two-dimensional planar flow. Their analytic curve showed that the axial flow Reynolds number at neutral stability increased linearly for large injection Reynolds numbers. Numerical calculations of Beddini[6] and the data he collected also displayed a linear neutral stability curve for large injection Reynolds numbers. Yamada et al.[3] performed hot-wire measurements of mean-velocity and turbulence-intensity profiles at several axial stations along a two-dimensional channel with uniform wall injection. They con-

Received March 12, 1990; revision received July 5, 1990; accepted for publication July 6, 1990.

*Graduate Student, Department of Power Mechanical Engineering.
†Professor, Department of Power Mechanical Engineering.

cluded that the laminar character of the mean flow would persist indefinitely at large axial distances. Contrary to the conclusion of Yamada et al., Beddini's numerical calculations[6] predicted a transition from a laminar to a turbulent-velocity profile at a certain axial distance. Laser-Doppler velocimetry (LDV) measurements of cold flow in a simulated two-dimensional nozzleless solid-rocket motor with constant wall injection were made by Traineau et al.[7] Their results revealed a mean-velocity profile transition, supporting Beddini's calculations.

Previous studies relevant to the case of nonuniform wall injections are comparatively scarce. Using the stream function method, Terrill[9] and Yuan and Brogren[10] obtained the axial velocity solutions for an open-end porous pipe flow, with wall injection distribution to be exponential functions. The constraints on the inlet conditions in their derivations were a fully developed impermeable pipe flow and small flows through the porous wall. Taylor[11] analytically analyzed the wedge and cone flows based on the Bernoulli's equation, and showed that nonuniform injection velocity distributions of the type x^p also yield similarity solution for axial velocity in the case of a very small wedge or cone angle. However, no information was given for transverse velocity, since the analysis was one-dimensional.

This literature survey reveals that most previous solutions were limited to uniform wall injection, thus, the associated experiments were set up so that the fluid injected from the wall had constant velocity. Moreover, previous studies pertinent to nonuniform wall injection were relatively sparse and restricted to the porous pipe with main flow, i.e., with an open fore-end. Furthermore, to simulate the actual propellant burning or erosive burning of a solid-rocket motor, ducts with a closed end, i.e., without main flow, and with nonuniform wall injection should be used.[4] However, this type of study is lacking both in experiment and theory. In view of these facts, it is clear that a study of the detailed flow characteristics in a closed-end porous-walled duct with nonuniform wall injection, both experimentally and analytically, would be worthwhile. This paper presents both the pressure data and the nonintrusively measured mean velocity and fluctuation results, using LDV for the flow development in such a configuration. Simple analytic expressions will also be derived to compare with the measured results. In particular, these questions are considered: 1) Can the similarity solution really be achieved in a closed-end duct with nonuniform lateral injection? 2) Is the transitional behavior of the flow analogous to the constant injection velocity case? Further, it is hoped that the results presented in this study will provide a useful data base, as well as additional information to the researchers in this area.

In this paper, the experimental system is stated first. The experimental conditions, including data accuracy, two-dimensionality, and symmetry of the flowfield, are subsequently provided. Then, the measured results are compared with the self-similar solutions derived in the Appendix. Mean-velocity profile transition, peak turbulence-intensity location, and evolution of relative turbulence intensity are also presented, and compared with previous studies of uniform wall injection in detail. Finally, a correlation of turbulence, heat transfer, and erosive burning rate is made.

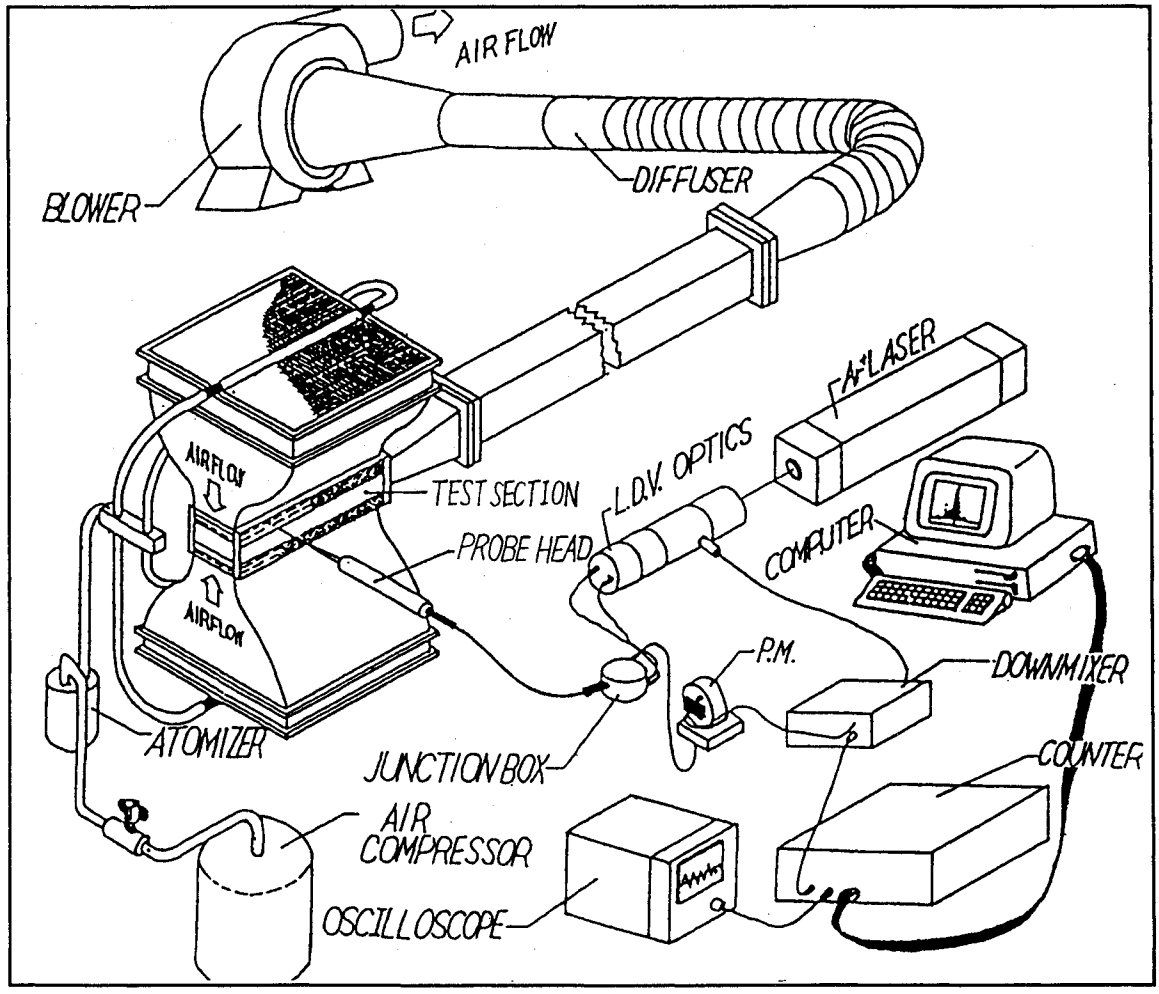

Fig. 1 Schematic drawing of overall experimental system.

Experimental Apparatus and Conditions

Experiment System

The closed-end porous duct and LDV experimental set-up is shown in schematic form in Fig. 1. Atmospheric air was drawn into each inlet through a flow straightener, three layers of wire screens in the settling chamber, and a 10:1 contraction by a turbo blower (3500 rpm/3 phase/10 hp) at the downstream end. Immediately, downstream of the contraction, three additional layers of wire screens with mesh numbers of 100, 100, and 200, respectively, were installed to simulate the porous wall of the test section. The simulated porous wall had a porosity of 90 μm and an open area ratio of 50%. Because the head end of the channel was closed, the channel flow was solely induced by wall mass addition, and the head end pressure was equal to the atmospheric one. The pressure upstream of the porous wall was uniform while the pressure downstream of it (i.e., the pressure distribution inside the channel) was decreasing with increasing axial distance; a nonuniform injection distribution along the porous wall could be anticipated. As will be stated later, this wall injection profile was near exponential, which could be viewed as an extreme variation relative to representative solid-rocket chamber flows. Figure 2 is a schematic drawing of the test section and coordinate system used. The closed head end and side walls of the test section were made of 10-mm Plexiglas; the test section was 417 mm long, 20 mm in height, and 60 mm wide. Downstream of the porous-walled test section, the air then flowed through a flow straightener, a rotameter (not shown in Fig. 1), and a bellows, and was exhausted by the blower driven by a dc motor with digital control circuits.

Two LDV systems were used to measure the mean-velocity and turbulence components in the porous-walled channel flow investigated. One was set up in a dual-beam forward or off-axis scattering configuration, with a 15-mW helium-neon laser as the light source. Its detailed optical arrangement was described in Liou and Wu[12] for a liquid-fueled ramjet combustor study. This LDV system was mainly used as an auxiliary instrument for near-wall ($Y = \pm h$) measurements with its long focal-length lens. The other was a dual-beam back scattering optical fiber LDV configuration. A linearly polarized 3-W argon ion laser (514.5 nm wavelength) provided the coherent light source. This beam was split into two parallel beams of equal intensity by a beamsplitter. A Bragg cell was used to cause a 40 MHz frequency shift on one of the beams. A frequency shift is used to eliminate the directional ambiguity. The resulting pair of beams was then directed into two single-mode polarization-preserving fibers. Within the fiber-optic probe, the laser beams from the two fibers were collimated and passed through a 102-mm focal-length lens. The focused beams entered the test section through the transparent plexiglas wall, intersected inside the duct (giving a probe volume with dimensions of 0.14 mm × 2.4 mm), and then passed through another side wall into the beam traps. The fiber-optic probe was mounted on a small milling machine with four vibration mounts. The light scattered from the seeding particles was collected by the aforementioned lens and a receiving lens and focused onto one multimode receiving fiber in order to deliver the scattered light to photomultiplier. The detected signal was electrically downmixed to the appropriate frequency shift (2–10 MHz in the present work). Then a counter processor with 2 ns resolution was used to process the Doppler signal. The Doppler signal was monitored on an oscilloscope and the digital output of the counter processor was fed directly to a PC/AT for storage and analysis. The seeding particles were introduced into each inlet air stream by a six-jet atomizer and a rake mounted on the top of the settling chamber. The atomizers were operated by filtered compressed air and salt water, and produced particles in the size range of 0.5–5 μm. The salt solution was mixed to give a nominal 0.8 μm particle after the droplet dried. The seeding flow rate was 74.7 (liters/min), and the seeding concentration was 1×10^6 (particles/cm^3).

A stainless tube of 0.6-mm inner diameter and 0.9-mm outer diameter served as a static-pressure probe to measure the local static pressure inside the test section through the holes on the side wall. This needle probe was then connected to one side of a strain-gage microdifferential transducer (Kyowa PDL-40B, ± 0.1%) that had another side opened to the atmospheric air. The measured pressure signal was subsequently amplified by a Kyowa WGA-200A amplifier and read from a digital readout. Note that the measured pressures could be directly interpreted as the channel axial pressure dropped from the head end, since the head-end pressure was essentially equal to the atmospheric one, as explained previously.

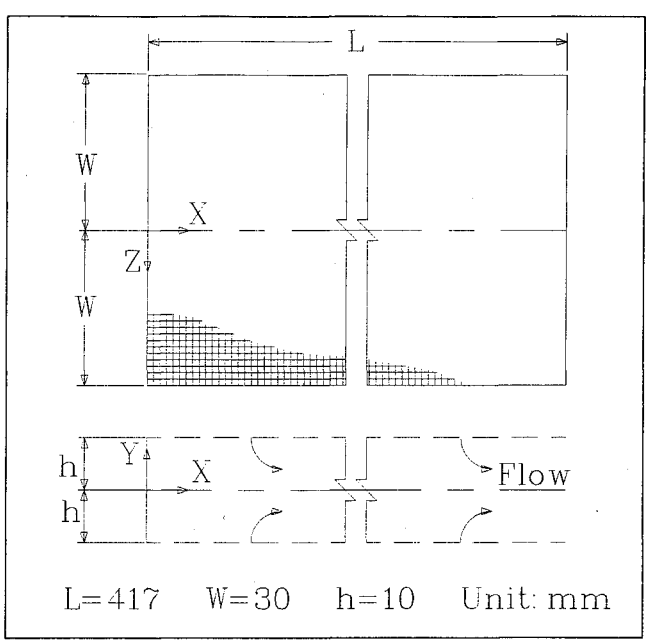

Fig. 2 Channel configuration and coordinate system.

Experimental Conditions

The velocity measurements were mainly carried out along the central plane ($Z/W = 0$) of the porous-walled duct, and were made at seven stations, i.e., $x = 20.85$, 31.65, 36.65, 39.15, 40.41, 41.03, 41.65. In each station, the measurements were made at 10–12 Y-locations. Table 1 is a list of flow conditions at two reference stations, corresponding to the first measurement station $x = 20.85$ and the near exit station $x = 41.65$, respectively. As can be seen, the maximum centerline Mach number in the duct is 0.254, which means the density variation of the air is less than $\Delta\rho/\rho \approx M^2/2 = 3.23\%$. Consequently, the entire flowfield in the porous-walled duct investigated is approximately incompressible. Table 1 further shows the conditions in Eqs. (A4) and (A5), such that ($|R_w| = R_{wi} \gg 1$, $|V_w/U_c| = V_{wi}/U_c \ll 1$, $|1 - U_c(0)/U_c| \leq x^2$, and $|1 - V_w(0)/V_w| \ll x^2$) are satisfied if x locates between 20.85 and 41.65. Therefore, there indeed exists a possibility of velocity similarity, as analyzed in the Appendix. The similarity will be further verified experimentally in the following section.

Since the transverse pressure gradients were relatively small, as compared to the axial one, the static pressure measurements inside the duct were made at 26 locations along the centerline. All the measured pressure data were relative to the head-end pressure.

Data Accuracy

The mean velocity and the turbulence intensity were calculated from the probability distribution function of the measurements described in Ref. 12. There were, typically, 4000

Table 1 Flow conditions at different sections (1 atm, 300 K)

x	U_c, m/s	V_{wi}, m/s	R_{wi}	V_{wi}/U_c	M_c	Air properties	
20.85	10.32	0.71	450	0.069	0.030	$R_a = 287$	J/Kg-K
						$\rho = 1.1774$	Kg/m³
41.65	88.30	7.91	5050	0.090	0.254	$\nu = 1.568 \times 10^{-5}$	m²/s

measurements at each measuring location. The corresponding statistical error was less than 1.3% in the mean velocity and less than 2.2% in the turbulent intensity, for a 95% confidence level. A constant time interval sampling mode was used to correct velocity bias.

Two-Dimensionality and Symmetry

The present experimental investigation was undertaken in a porous-walled duct with an aspect ratio of 3. An aspect ratio of 2 was previously used by Traineau et al.[7] to simulate a nozzleless solid-rocket motor. In the present work, a check of two dimensionality of the flowfield was made at various axial stations. The results show that both mean velocity and pressure are two-dimensional over the center 48 mm of its width (60 mm, Z-direction), to within 2.3%. The data presented in the foregoing sections are those taken in the $Z = 0$ plane. The symmetry of the flow pattern was also examined at various axial stations. Both the axial mean-velocity and static-pressure profiles at two selected axial stations, $x = 20.85$ (i.e., duct half-length) and $x = 41.65$ (i.e., duct exit), are displayed in Fig. 3, and reveal good symmetry. Consequently, the data presented in the previous sections are those taken in one-half of the $Z = 0$ plane.

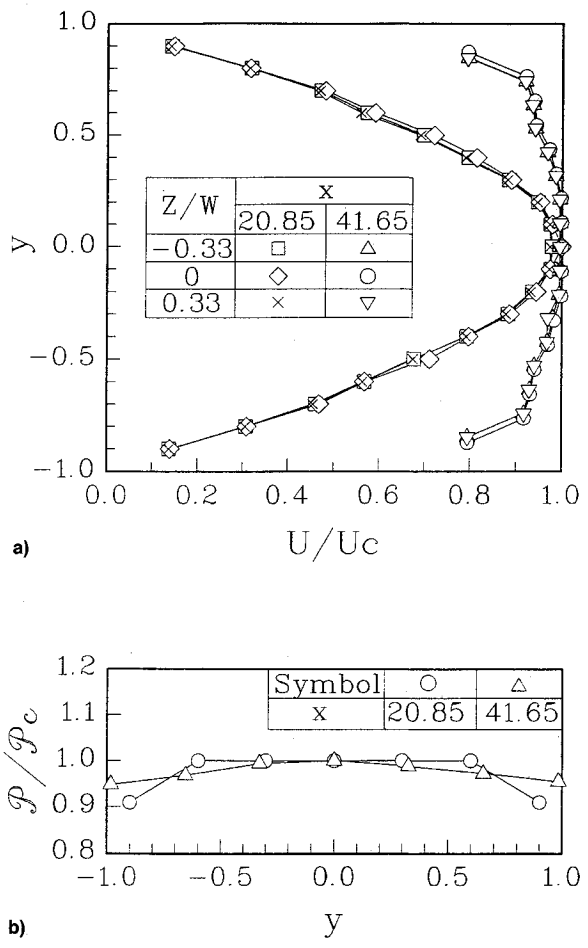

Fig. 3 Transverse distributions of normalized (a) axial mean velocity and (b) static-pressure drop at $x = 20.85$ and 41.65.

Results and Discussion

Distributions of Pressure, Injection Velocity, and Centerline Velocity

Figure 4 depicts the measured pressure drop along the duct centerline, $\mathcal{P}_c(x)$. The solid line in Fig. 4 is the curve-fitted line through the measured data ($12.21 \le x \le 38.13$), and can be expressed by the following form, according to Eq. (A22):

$$\mathcal{P}_c^{1/2} + (\mathcal{P}_c - 7.89)^{1/2} = 16.31 \exp[0.1254(x - 20.85)] \quad (1)$$

Equation (1) is then used to calculate the distributions of wall injection mean velocity V_{wi}, centerline axial mean velocity U_c, and V_{wi}/U_c ratio, through Eqs. (A23), (A26), and (A28). The calculated results are compared with the experimental data in Figs. 5–7. It is seen that the calculated and

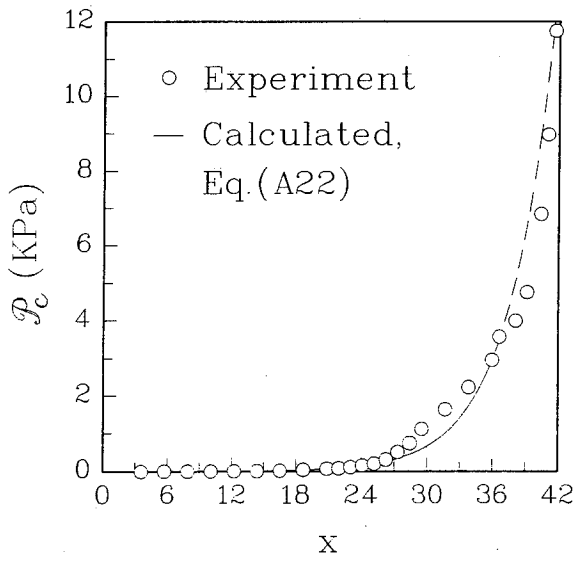

Fig. 4 Distribution of pressure drop along the centerline.

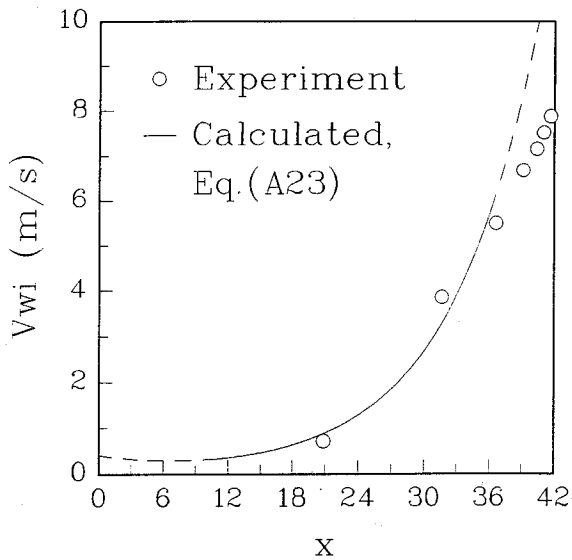

Fig. 5 Distribution of wall injection mean-velocity in plane $Z = 0$.

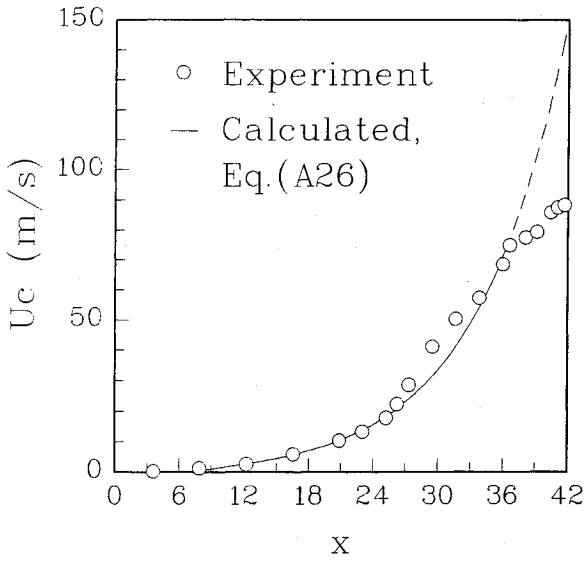

Fig. 6 Distribution of centerline axial-mean velocity.

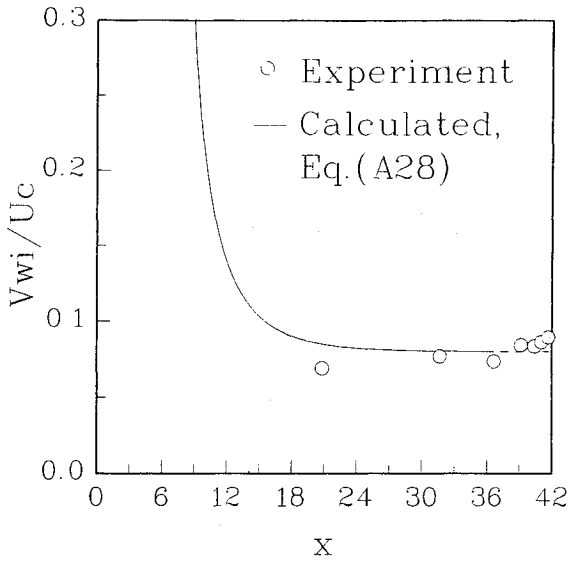

Fig. 7 Distribution of local injection ratio in plane Z = 0.

measured trends are in reasonable agreement, except for $x > 36.65$, where the calculated results of U_c and V_{wi}/U_c progressively depart from the experimental data, due to the transition of the mean-velocity field from laminar to turbulent profile. Additionally, Fig. 7 shows that, as x increases, V_{wi}/U_c, first, decreases rapidly and, then, remains approximately constant with a value of 0.069 ~ 0.090 for $x \geq 20.85$.

Mean-Velocity Profiles

The measured axial and transverse mean-velocity profiles at various axial stations are shown in Figs. 8 and 9, respectively. The normalized velocity profiles for $x = 20.85$, 31.65, and 36.65 reveal the similarity feature, and are in good agreement with the laminar theory given by Eqs. (A27) and (A24), as denoted by the solid lines in the figures. At about $x = 39.15$, the measured mean-velocity profiles have begun to depart from laminar theory. The profiles continue to develop in steepness of near-wall gradient, such that, by the exit section [$x = 41.65$ ($M_c = 0.254$)], the turbulent mean-velocity profile is even flatter than that of 1/7 power law (denoted as dash line in Fig. 8) of the fully developed turbulent pipe flow. For the case of uniform wall injection, extrapolating the experimental results of Yamada et al.,[3] Beddini[6] calculated the

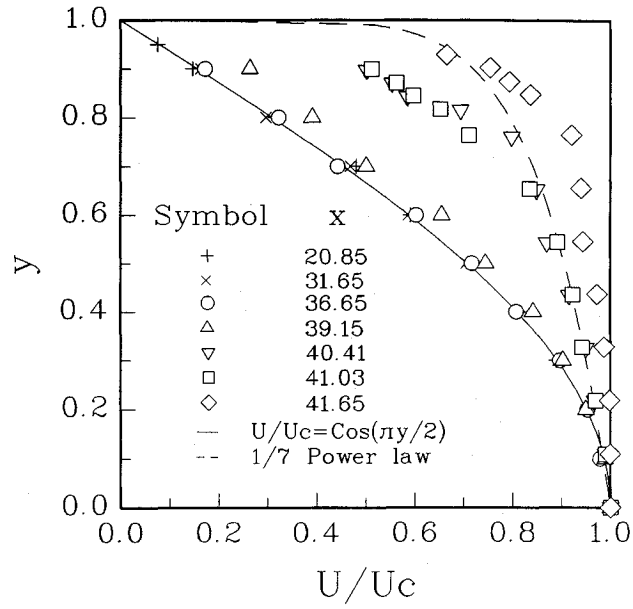

Fig. 8 Normalized axial mean velocity profiles at various axial stations (V_{wi} = 0 ~ 7.9 m/s).

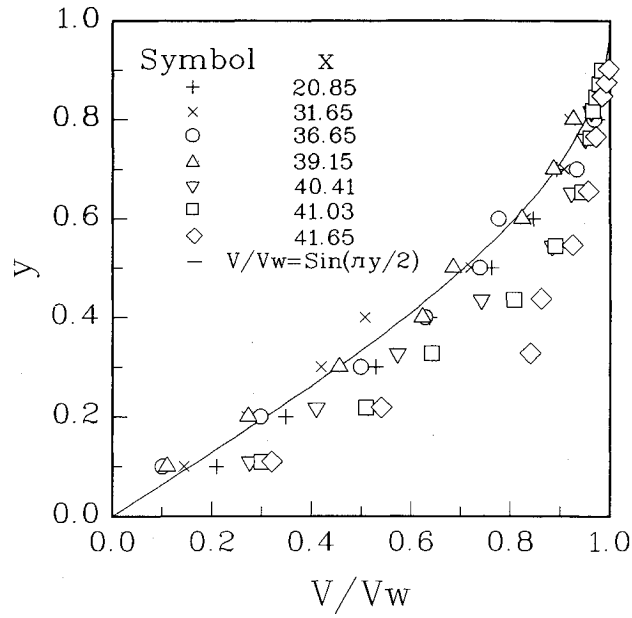

Fig. 9 Normalized transverse mean velocity profile at various axial stations (V_{wi} = 0 ~ 7.9 m/s).

variation of incompressible axial mean-velocity profile for higher x, and showed a 1/5 power law profile at $x = 130$ ($M_c \approx 0.6$). Similarly, Traineau et al.[7] reported an axial turbulent mean-velocity profile with a gradient near the wall lower than that of 1/7 power law at the throat ($x = 45.5$, $M_c = 1$) of a simulated nozzleless rocket motor. Obviously, all the flowfields just mentioned have not attained full development completely.

To investigate the possibility of velocity similarity in fully turbulent region, a similar form of U-profile is assumed as

$$U(x, y)/U_c(x) = (1 - y)^n \tag{2}$$

From the continuity equation and the boundary conditions of $V(x, 0) = 0$ and $V(x, 1) = V_w(x)$, one obtains

$$V(x, y)/V_w(x) = 1 - (1 - y)^{n+1} \tag{3}$$

For n = ⅕ or smaller, as the experiment had shown, Eq. (3) shows that the similarity profile of V/V_w will deviate from the curve of $\mathrm{Sin}(\pi y/2)$ in the opposite side of being a fuller one. This trend conflicts with the experimental result shown in Fig. 9. As a matter of fact, it is concluded that the normalized mean-velocity profiles in the turbulent zone will be varying with x and, therefore, no velocity similarity exists in the turbulent zone at all.

It may be worth mentioning here that the difference in the reported axial turbulent mean-velocity profiles between the Traineau et al.[7] and present experiments is in part due to the different injection distribution and in part due to compressibility. The experiment of Traineau et al. was intended to simulate a choked nozzleless rocket motor and, therefore, the compressibility had some effects on the flow pattern in the turbulent regime where the flow Mach number varied from 0.5 to 1. In their experiment, the uniform injection resulted in a decrease of V_{wi}/U_c, from 0.19 to 0.03 in the laminar similarity region, where velocity similarity preserved, and from 0.03 to 0.01 in the transition and turbulent regimes, respectively. In contrast to their work, the wall injection profile in the present work is approximately exponential, and the corresponding V_{wi}/U_c remains nearly constant, with a value of 0.07 ± 0.01 (Fig. 7) in the pertinent region ($x \geq 20.85$). Consequently, the local injection ratio, V_{wi}/U_c, is one of the major factors determining the steepness of the wall gradient of the turbulent mean-velocity profile investigated.

Transition Phenomena

In order to estimate the length of the transition region from the measured data, the integral momentum flux factor β is plotted vs normalized axial distance in Fig. 10, where the results predicted by laminar similarity theory is also included for comparison. The experimental data are seen to agree with laminar theory up to x = 36.65. This trend is consistent with the observation previously made from Figs. 5–6 and 8–9. As the flow proceeds further downstream, β drops rapidly below the laminar theory, by 15% at x = 41.65, and attains the value of 1.03 at $x \approx 42$ (i.e., exit). It is worth mentioning here that theoreticians in related technical fields (viz., solid propulsion) have hypothesized the fully turbulent-velocity profile behavior for porous-walled duct flow by analogy to either impermeable tube flows (β = 1.03) or flat-plate boundary-layer flows (β = 1.02).[13] For the case of tube flows with uniform injection, Beddini's calculations[6,13] and experiments by Olsen and Ecker[14] and Ecker and Rodi[15] showed that β indeed asymptoted to the value of the impermeable tube (1.03) as the flow approached full turbulence. When the β-value drops to the vicinity of 1.03, as indicated by Fig. 10,

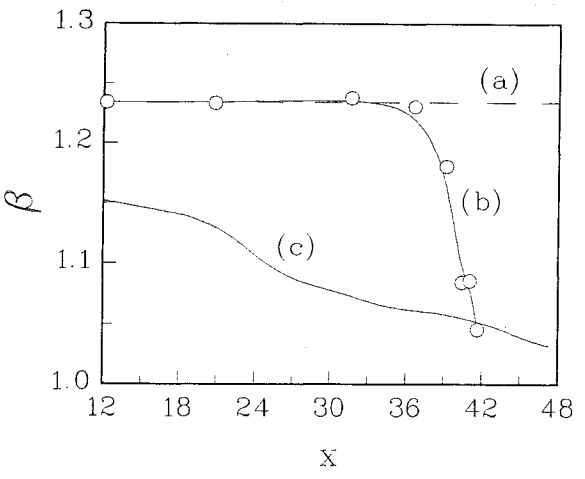

Fig. 10 Behavior of momentum flux factor as a function of axial position (a) laminar theory, β = 1.234 (b) present, V_{wi} = 0 ~ 7.9 m/s ($\bar{V}_{wi}$ = 1.9 m/s) (c) Traineau et al.[7], V_{wi} = 3.1 m/s.

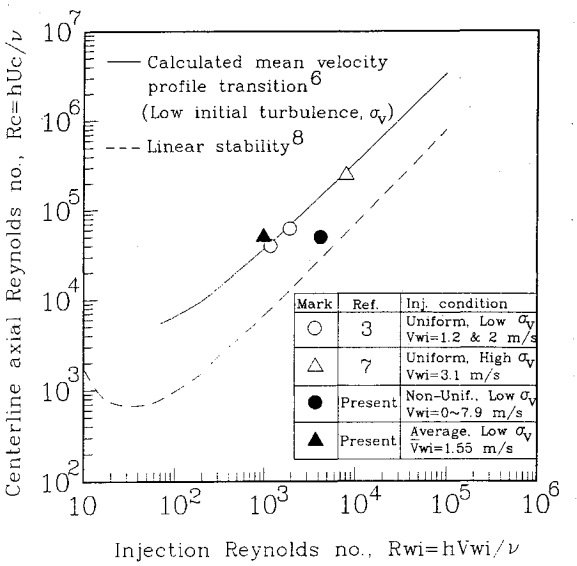

Fig. 11 Variation of centerline axial Reynolds number with injection Reynolds number for mean axial velocity transition under uniform wall injection.

it is reasonable to consider the present flow as near fully turbulent at $x \approx 42$. Thus, the length of the mean-flow transition process is seen to be of the order of 5.4 duct half-heights. The length of the mean-flow transition process defined in this way was of the order of 5–10 radii for porous-walled duct flow, as predicted by Beddini.[13]

The foregoing discussion indicates that the momentum flux factor β is a useful parameter for identifying the transition phenomena. Another way to study the transition phenomena is to evaluate the centerline axial Reynolds number R_c at which the measured mean-velocity profile transition occurs, $x > 36.65$, according to Fig. 10, and then compare that with the theoretical curve predicted by Beddini.[6,13] Such a comparison is depicted in Fig. 11, where the linear stability curve of Varapaev and Yagodkin,[8] as well as the experimental results of Yamada et al.[3] and Traineau et al.[7] for constant wall injection, are also included for comparison. Note that the prediction of Beddini is under the assumption of constant-wall injection (R_{wi} = const), whereas the present experiment is under nonuniform injection ($R_{wi} \neq$ const). As a result, it may be more appropriate to adopt two injection Reynolds numbers; one is the local R_{wi} at x = 36.65 (solid circle in Fig. 11) and the other is the average injection Reynolds number before transition, $\bar{R}_{wi}$ (solid triangle in Fig. 11). As can be seen from Fig. 11, the experimental data using $\bar{R}_{wi}$ is in a better agreement with the theoretical curve predicted by Beddini.[6] Consequently, the mean flow investigated in the present study indeed begins the transition at $x > 36.65$.

Turbulence-Intensity Profiles

Figure 12 depicts the turbulence-intensity profiles at various axial stations for the present nonuniform injection case (V_{wi} = 0 to 7.9 m/s). It is seen in Fig. 12 that the flow is actually turbulent, with local turbulence levels ranging up to 4% of the local centerline mean velocity in the so-called laminar similarity region ($x \leq 36.65$), where the mean-velocity profiles maintain their laminar form and possess similar property, as has been shown in Figs. 8 and 9 and proven in the Appendix. This behavior is due to the stability effect of the large and favorable axial pressure gradient found in the porous-walled duct flow investigated (Fig. 4). There are several more features found from Fig. 12. The level of the turbulence intensity profile at a given axial station increases with increasing axial distance. The increase is gradual in the laminar similarity region ($x \leq 36.65$), whereas the increase is particularly rapid

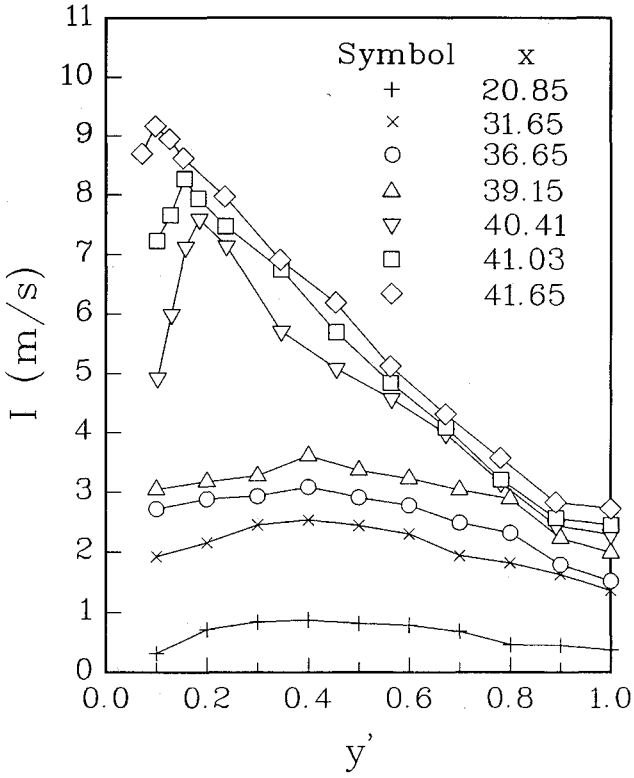

Fig. 12 Turbulence intensity profiles at various axial stations.

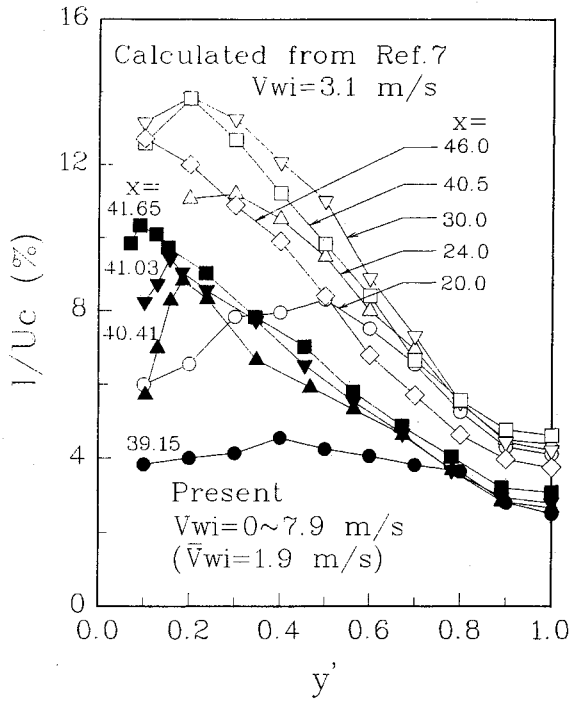

Fig. 13 A comparison of normalized turbulence intensity profiles in the transition process measured by different researchers.

in the transition region ($x > 36.65$). Moreover, the turbulence-intensity profile at a given station exhibits a peak. For the laminar similarity region, the peaks all appear midway between the channel centerline and the porous surface, where the laminar mean-velocity profiles have the steepest gradient (Figs. 8 and 9). However, for the transition region, the turbulence-intensity peak is moving closer to the wall, from $y' = 0.4$ to $y' = 0.1$, with increasing axial distance, since the corresponding mean-velocity profile is becoming more and more flat around the duct centerline and more and more steep near the porous surface (Figs. 8 and 9). This later feature has also been obseved by other investigators under a uniform injection condition,[3,6,7] and is important to the burning mechanism of a solid propellant grain. The maximum turbulence intensity, occurring adjacent to the porous surface, is to enhance not only the heat transfer rate but also the mixing rate of decomposition gases, so that the burning rate is augmented.

It is interesting to make a comparison of the present turbulence-intensity profiles normalized by the local centerline mean velocity with those reported by Traineau et al.[7] under uniform injection conditions. This is plotted in Fig. 13. Different trends are found between the two experiments. For the present experiment, I/U_c at a given axial station is always increasing, with increasing axial distance, whereas the I/U_c data of Traineau et al.[7] first show an increase in the transition region ($20 \leq x \leq 30$) and then a decrease in the turbulent region ($x > 30$), as the axial distance is increased. The decrease in their I/U_c data in the turbulent region was attributed to the effect of compressibility. Additionally, in the authors' opinion, the opposite trends of I/U_c profiles are attributed to both the injection profile and the V_{wi}/U_c ratio discussed in the previous section. For a closed-end channel with wall injection, the increase of I is mainly due to the transition process associated with flow acceleration, and to the interaction between the wall injection jets and main flow. Downstream of the transition region, the increase of I results mainly from the latter factor, which is characterized by V_{wi}/U_c. In the experiment of Traineau et al.,[7] V_{wi}/U_c was found to decrease with x; therefore, the enhancement of I may be unable to catch up with that of U_c, and a decrease of I/U_c with increasing x is possible. On the other hand, the compressibility is negligibly small, the flow is developed up to transition stage only, and the V_{wi}/U_c ratio is approximately constant in the present experiment. These facts illustrate why I/U_c is progressively increased, with increasing x in the present work.

Turbulence, Heat Transfer, and Erosive Burning

For practical applications, it is certainly worthwhile to correlate the relationship between the turbulence intensity, heat transfer rate, and erosive burning rate. According to the present experiment, the following relationship (Fig. 14) is found for the near-wall gradient of peak turbulence intensity.

$$I_p/Y'_p \propto (U_b^{0.8}/h^{0.2}) \exp(-\beta_e V_{wi}/U_b) \qquad (4)$$

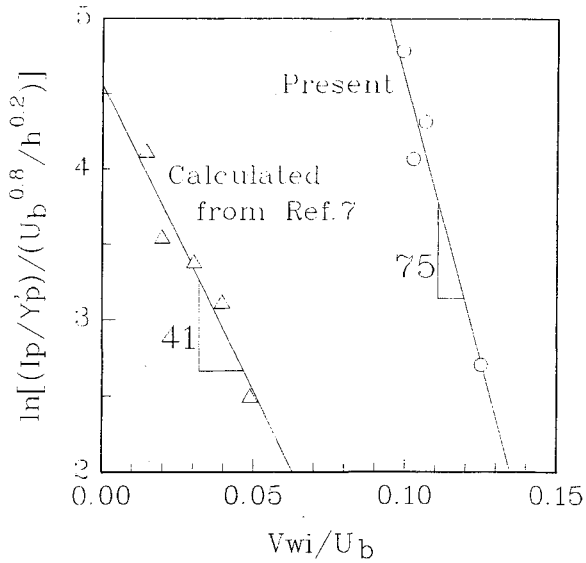

Fig. 14 Correlation between $[(I_p/Y'_p)/(U_b^{0.8}/h^{0.2})]$ and V_{wi}/U_b in transition and turbulent zones (units: M.K.S.).

Table 2 Estimation of force ratios on a fluid element

x		20.85	31.65	36.65
$(F_v/F_p)_{max}$		0.84%	0.11%	0.07%
$(F_r/F_p)_{max}$	<	2.8%	0.36%	0.27%

A similar relation was also found by Yamada et al.[3] for a circular tube flow with constant wall injection. However, in that correlation, the U_b in Eq. (4) was replaced by U_c. The significance of Eq. (4) is that its right-hand side is proportional to $(\hbar h)/\lambda$ and, therefore, is exactly the same form as the heat transfer equation for a duct flow with $P_r \approx 1$. A heat transfer equation similar to Eq. (4) was adopted by Lenoir and Robillard[16] to describe the augmented burning effect of a solid propellant rocket motor under erosive burning conditions. Consequently, the near-wall turbulence gradient I_p/Y'_p has intimate correlation with heat transfer and erosive burning of a solid propellant rocket motor.

The proportional constant β_e in Eq. (4) varies with the injection velocity profile. An example is shown in Fig. 14, where $\beta_e = 41$ is for the uniform injection case calculated from the raw data of Traineau et al.,[7] and $\beta_e = 75$ is for the nonuniform injection case of the present work. Note that these two values of β_e are within the common range of $40 \leq \beta_e \leq 120$ for erosive burning of solid propellants. However, if the decreasing rate of V_{wi}/U_b in the transition process were the same, a larger value of β_e, as in the present work, would imply a larger change of I_p/Y'_p and, subsequently, a larger augmentation of the heat transfer rate or erosive burning rate of solid propellants. In addition, Fig. 14 indicates that the bulk axial velocity U_b, adopted in Eq. (4), is suitable for both uniform and nonuniform wall injections. Nevertheless, the centerline axial velocity U_c, adopted by Yamada et al.[3] in Eq. (4), is found to be unsuitable for the case of nonuniform wall injection.

Validity of Equations

In the Appendix, an X-momentum equation was reduced to inviscid Euler form [Eq. (A6)]. The validity of this equation and its solution requires that the ratio of the resultant force of viscous and Reynolds stresses to the pressure force be relatively small, and is worth further discussion.

Consider a small fluid element. Let F_v, F_r, and F_p denote forces acting on it by viscous stress, Reynolds stress, and pressure, respectively. Then

$$F_v/F_r \approx \left| \frac{\partial}{\partial Y}\left(\mu \frac{\partial U}{\partial Y}\right) \Big/ \left(\frac{\partial P}{\partial X}\right) \right| \tag{5}$$

$$F_r/F_p \approx \left| \frac{\partial}{\partial Y}(-\rho\overline{u'v'}) \Big/ \left(\frac{\partial P}{\partial X}\right) \right| \leq \left| \frac{\partial}{\partial Y}(\rho uv) \Big/ \left(\frac{\partial P}{\partial X}\right) \right| \tag{6}$$

Table 2 is an estimation of force ratios on a fluid element. As can be seen, the maximum order of $(F_v + F_r)/F_p$ is no more than 3.6% in the region $x = 20.85 \sim 36.65$. This result supports the theoretical analysis given in the Appendix.

Summary and Conclusion

This paper presents the results of an investigation of the flowfield in a closed-end porous-walled duct with nonuniform fluid injection. The lateral injection velocity profile, due to a minimal pressure drop across the duct surface designed in this experiment, is nearly exponential, and may represent an extreme variation relative to representative solid-rocket chamber flows. Additionally, an approximately similar solution has been theoretically derived under some appropriate conditions that can be reduced to $R_{wi} \geq 450$ and $V_{wi}/U_c \leq 0.09$, according to the present experimental data. The deduced wall injection and centerline mean-velocity distributions, as well as axial and transverse mean-velocity profiles, are in reasonable agreement with the LDV measured data for the flow regime upstream of the mean-velocity profile transition ($20.85 \leq x \leq 36.65$).

A comparison of flow characteristics between the present nonuniform and previous uniform wall injections has been made. Both cases show a fast increase of the turbulence level, a continuous shift of peak turbulence intensity toward the porous walls, and a progressive departure from the self-similar mean-velocity profile as the axial distance is increased in the transition flow regime. However, the decrease of the relative turbulence intensity I/U_c, with x found in the case of uniform wall injection, does not appear in the present nonuniform wall injection case. In addition to the effect of compressibility, the difference in the distribution of the relative injection ratio V_{wi}/U_c, which remains approximately invariant in the latter case but decreases with x in the former, is proposed to be the main reason for the above difference in I/U_c behavior between the two cases. For both cases, the near-wall gradient of peak turbulence intensity is found to be proportional to the heat transfer rate and, also, to the erosive burning rate, with the proportional constant β_e falling in the common range of solid-propellant erosive burning. Furthermore, owing to the nearly exponentially increased injection profile, β_e, for the present case, is larger than that for the uniform injection case in the transition flow regime. Consequently, for a given decreasing rate of V_{wi}/U_b, the present case provides a larger augmentation of heat transfer or erosive burning rate. This comparison reveals that β_e, usually treated as a constant in the Lenoir-Robillard erosive burning model, is actually affected by the wall injection profile.

In the present experiment, both the measured momentum flux factor and centerline axial Reynolds number depict the existence of the transition flow regime. Nevertheless, to display the fully developed turbulent flow regime, the duct would require lengthening. A more rigorous prediction of the variation of centerline axial Reynolds number for mean-velocity transition with injection Reynolds number under nonuniform wall injection would also be highly desirable for comparison with the present measurements.

Appendix: Derivation of Similar Solution

The system of equations describing a two-dimensional, steady, laminar, and incompressible flow with neglecting body force can be written in the form

$$\frac{\partial U}{\partial x} + \frac{\partial V}{\partial y} = 0 \tag{A1}$$

$$U\frac{\partial U}{\partial x} + V\frac{\partial U}{\partial y} = -\frac{1}{\rho}\frac{\partial P}{\partial x} + \frac{\nu}{h}\left(\frac{\partial^2 U}{\partial x^2} + \frac{\partial^2 U}{\partial y^2}\right) \tag{A2}$$

$$U\frac{\partial V}{\partial x} + V\frac{\partial V}{\partial y} = -\frac{1}{\rho}\frac{\partial P}{\partial y} + \frac{\nu}{h}\left(\frac{\partial^2 V}{\partial x^2} + \frac{\partial^2 V}{\partial y^2}\right) \tag{A3}$$

Consider a duct with nonuniform and symmetric lateral injection and with a main flow (i.e., with an open fore-end). Referring to the coordinate system shown in Fig. 2, and applying order of magnitude analysis to Eqs. (A1)–(A3), one gets $|\partial P/\partial y| \ll |\partial P/\partial x|$ if

$$|1 - V_w(0)/V_w| \ll x^2,\ |V_w/U_c| \ll 1 \text{ and } |R_w| \geq 1 \tag{A4}$$

That is, the Y-momentum equation can be neglected. Additionally, if

$$|1 - U_c(0)/U_c| \leq x^2 \quad \text{and} \quad |R_w| \gg 1 \tag{A5}$$

then X-momentum equation reduced to the inviscid Euler's form

$$U\frac{\partial U}{\partial x} + V\frac{\partial U}{\partial y} = -\frac{1}{\rho}\frac{dP}{dx} \tag{A6}$$

Note that, in suction flows, U_c is a decreasing function of x (i.e., $U_c \leq U_c(0)$). The second condition given by Eq. (A4) and the first condition given by Eq. (A5) are hard to satisfy when the flow has proceeded a long distance. On the contrary, U_c is always an increasing function in injection flows [i.e., $U_c \geq U_c(0)$], so that Eqs. (A4) and (A5) may be satisfied as x increases to make Eq. (A6) valid.

Introducing the stream function Ψ, the following form is assumed for a similar solution:

$$\Psi(x, y) = g(x)f(y) \tag{A7}$$

hence,

$$U(x, y) = \frac{1}{h}\frac{\partial \Psi}{\partial y} = \frac{gf'}{h} \tag{A8}$$

$$V(x, y) = -\frac{1}{h}\frac{\partial \Psi}{\partial x} = -\frac{g'f}{h} \tag{A9}$$

Equation (A6) then becomes

$$f'^2 - ff'' = -\frac{h^2}{\rho g g'}\frac{dP}{dx} = \text{constant} \tag{A10}$$

Differentiating Eq. (A10) with respect to x gives

$$f'f'' - ff''' = 0 \tag{A11}$$

which can be integrated to

$$f(y) = \sin(\pi y/2) \tag{A12}$$

with the following boundary conditions:

$$\text{At wall, } U(x, 1) = 0 \quad \text{or} \quad f'(1) = 0 \tag{A13}$$

$$V(x, 1) = V_w \quad \text{or} \quad V_w = -g'/h \quad \text{if} \quad f(1) = 1 \text{ is assigned} \tag{A14}$$

(mathematically, $f(1)$ can be any constant)

$$\text{along centerline, } \frac{\partial}{\partial y}U(x, 0) = 0 \quad \text{or} \quad f''(0) = 0 \tag{A15}$$

$$V(x, 0) = 0 \quad \text{or} \quad f(0) = 0 \tag{A16}$$

$$\text{gross mass balance, } U_b(x) = \int_0^1 U(x, y)dy = \frac{g(x)}{h} \tag{A17}$$

Note that Eq. (A13) also implies normal injection at wall.

Assume the similar solution existing between station x_1 and x. Substituting Eq. (A12) into Eq. (A10) and integrating from x_1 to x, with integration constant determined by the use of Eq. (A17), one obtains

$$g(x) = \frac{2h}{\pi}\left\{\frac{2}{\rho}\left[\mathcal{P}(x) + q_1\right]\right\}^{1/2} \tag{A18}$$

$$\text{where} \quad q_1 = (\pi/2)^2\rho U_{b1}^2/2 - \mathcal{P}_1 = \rho U_{c1}^2/2 - \mathcal{P}_1 \tag{A19}$$

$$\text{and} \quad \mathcal{P}(x) = P_0 - P(x) \tag{A20}$$

For the present experiment, the injection velocity, $-V_w$ or V_{wi}, will be determined by the pressure loss across the simulated porous wall. Because multiple layers of wire screens were used, the pressure drop across the screens may be assumed as

$$\Delta P = P_{atm} - P(x) = P_0 - P(x) = \mathcal{P}(x) = C_p\rho V_w^2/2 \tag{A21}$$

where P_{atm} is the uniform stagnation pressure outside the porous walls and C_p is a constant to be determined by the experiment. Also, if the channel head-end is closed, P_{atm} will be equal to the channel head-end pressure P_o. Combining Eqs. (A14), (A18), and (A21), and integrating from x_1 to x, one gets

$$\frac{\mathcal{P}^{1/2} + (\mathcal{P} + q_1)^{1/2}}{\mathcal{P}_1^{1/2} + (\mathcal{P}_1 + q_1)^{1/2}} = \exp[\pi(x - x_1)/(2C_p^{1/2})] \tag{A22}$$

The distributions of transverse and axial mean velocities will then be expressed as

$$V_{wi}(x) = -V_w(x) = [2\mathcal{P}(x)/(\rho C_p)]^{1/2} \tag{A23}$$

$$V/V_w = \sin(\pi y/2) \tag{A24}$$

$$U(x, y) = \{(2/\rho)[\mathcal{P}(x) + q_1]\}^{1/2}\cos(\pi y/2) \tag{A25}$$

$$U_c(x) = U(x, 0) = \{(2/\rho)[\mathcal{P}(x) + q_1]\}^{1/2} \tag{A26}$$

$$U/U_c = \cos(\pi y/2) \tag{A27}$$

$$V_{wi}/U_c = \{[\mathcal{P}(x)/C_p]/[\mathcal{P}(x) + q_1]\}^{1/2} \tag{A28}$$

It is seen from Eqs. (A22) and (A23) that the wall injection profile, $V_{wi}(x)$, is roughly exponential.

Note that this derivation is based on the assumption of laminar flow. For injection-induced flow, especially at high R_{wi}, the flow is usually turbulent. As long as the net force, due to Reynolds stress acting on a fluid element, is small compared to the net pressure force, the axial momentum equation will still reduce to the same inviscid Euler form [Eq. (A6)], and Eqs. (A22)–(A28) will be valid, too. The analysis based on experimental data by Dunlap et al.[2] has confirmed this argument.

Acknowledgments

Support for this work was provided by the National Science Council of the Republic of China under contract number CS77-0210-D007-11.

References

[1]Culick, F. E. C., "Rotational Axisymmetric Mean Flow and Damping of Acoustic Waves in a Solid Propellant Rocket," *AIAA Journal*, Vol. 4, No. 8, 1966, pp. 1462–1464.

[2]Dunlap, R., Willoughby, P. G., and Hermsen, R. W., "Flowfield in the Combustion Chamber of a Solid Propellant Rocket Motor," *AIAA Journal*, Vol. 12, No. 10, 1974, pp. 1440–1442.

[3]Yamada, K., Goto, M., and Ishikawa, N., "Simulative Study on the Erosive Burning of Solid Rocket Motors," *AIAA Journal*, Vol. 14, No.9, 1976, pp. 1170–1176.

[4]Razdan, M. K., and Kuo, K. K., "Erosive Burning Study of Composite Solid Propellants by Turbulent Boundary-Layer Approach," *AIAA Journal*, Vol. 17, No. 11, 1979, pp. 1225–1233.

[5]Beddini, R. A., "Aerothermochemical Analysis of Erosive Burning in a Laboratory Solid-Rocket Motor," *AIAA Journal*, Vol. 18, No. 11, 1980, pp. 1346–1353.

[6]Beddini, R. A., "Injection Induced Flows in Porous-Walled Ducts," AIAA Paper 85-1406, July 1985.

[7]Traineau, J-C., Hervat, P., and Kuentzmann, P., "Cold-Flow Simulation of a Two-Dimensional Nozzleless Solid Rocket Motor," AIAA Paper 86-1447, June 1986.

[8]Varapaev, V. N., and Yagodkin, V. I., "Flow Stability in a Channel With Porous Walls," *Izvestiya. Akademii Nauk Soyuz Sovetskikh Sotsialisticheskikh Respublik (Union of Soviet Socialist Republics), Mekhanika Zhidkosti i Gaza*, Vol. 4, No. 5, 1969 pp. 91–95, translated in *Fluid Dynamics*.

[9]Terrill, R. M., "An Exact Solution for Flow in a Porous Pipe," *Journal of Applied Mathematics and Physics* (*ZAMP*), Vol. 33, No. 4, 1982, pp. 547–552.

[10]Yuan, S. W., and Brogren, E. W., "Turbulent Flow in a Circular Pipe with Porous Wall," *The Physics of Fluids*, Vol. 4, No. 3, 1961, pp. 368–372.

[11]Taylor, F. R. S., Sir Geoffrey, "Fluid Flow in Regions Bounded by Porous Surfaces," *Proceedings of the Royal Society of London, England*, Vol. A234, No. 1199, 1956, pp. 456–475.

[12]Liou, T.-M., and Wu, S.-M., "Flowfield in a Dual-Inlet Side-Dump Combustor," *Journal of Propulsion and Power*, Vol. 4, No. 1, 1988, pp. 53–60.

[13]Beddini, R. A., *Analysis of Injection-Induced Flows in Porous-Walled Ducts with Application to the Aerothermochemistry of Solid-Propellant Motors*, Ph.D. Thesis, Rutgers Univ., New Brunswick, NJ, Oct. 1981.

[14]Olsen, R. M., and Ecker, E. R. G., "Experimental Studies of Turbulent Flow in a Porous Circular Tube with Uniform Fluid Injection Through The Tube Wall," *Journal of Applied Mechanics*, Vol. 33, No. 1, 1966, pp. 7–17.

[15]Eckert, E. R. G., and Rodi, R., "Reverse Transition Turbulent-Laminar for Flow Through a Tube with Fluid Injection," *Journal of Applied Mechanics*, Vol. 35, No. 4, 1968. pp. 817–819.

[16]Lenoir, J. M., and Robillard, G., "A Mathematical Method to Predict the Effects of Erosive Burning in Solid-Propellant Rockets," *6th International Symposium on Combustion*, at Yale University, New Haven, Connecticut, August 19–24, 1956. Reinhold Publishing Corporation, N.Y., pp. 663–667.